Environmental Science & Technology

pubs.acs.org/est

Article

Quantitative Enhancement of Arsenate Immobilization Induced by Vacancy Defects on Various Exposed Lattice Facets of Hematite

Juan Liu, Jingtao Hou,* Juan Xiong, Lu Ren, Mingxia Wang, Wenfeng Tan, and Andreas Kappler

Cite This: *Environ. Sci. Technol.* 2025, 59, 2802−2814

Read Online

ACCESS | Metrics & More | Article Recommendations | Supporting Information

ABSTRACT: Defects are common features in hematite that arise from deviations from the perfect mineral crystal structure. Vacancy defects have been shown to significantly enhance arsenate (As) immobilization by hematite. However, the contributions from vacancy defects on different exposed facets of hematite have not been fully quantified. In this study, hematite samples with various morphologies were pretreated with sodium borohydride ($NaBH_4$) to generate oxygen vacancy defects (OVDs), analyzed quantitatively using extended X-ray absorption fine structure (EXAFS) and thermogravimetric analysis (TG). Batch experiments revealed that the OVDs on different exposed facets showed significant variations in improving arsenate adsorption, i.e., the quantitative enhancement of arsenate adsorption amount per unit OVD concentration ($\Delta Q_m/C_{defect}$) followed the sequence of (110) facet (80.05 μmol/mmol$_{def}$) > (001) facet (31.85 μmol/mmol$_{def}$) > (012) facet (13.14 μmol/mmol$_{def}$). The underlying mechanism by which OVDs affect arsenate adsorption across different exposed facets of hematite was studied. The results reveal that the tremendous improvement of arsenate adsorption caused by OVDs on the (110) facet compared to (001) and (012) facets was attributed to their stronger bonding strength of As to under-coordinated Fe atoms, thus significantly promoting the immobilization of arsenate. The findings of this study enhance our ability to precisely understand the migration and fate of As while also aiding in the design of highly efficient iron mineral materials for mitigating As pollution.

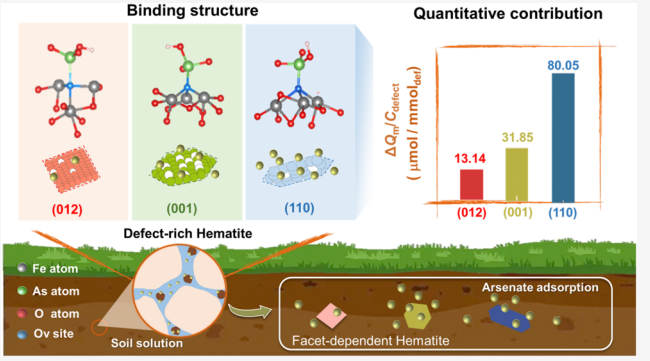

KEYWORDS: *hematite, vacancy defect, morphology, arsenate, immobilization*

1. INTRODUCTION

The contamination of arsenic (As) in the environment has emerged as a serious issue due to its high toxicity and carcinogenicity, posing significant risks to human health and the biosphere.[1,2] The retardation of As by minerals through reduction, adsorption, or precipitation mechanisms is one of the dominant natural processes to affect the migration and fate of As.[3,4] Hematite (α-Fe_2O_3) is a natural and thermodynamically stable phase of iron oxides with high reactivity, which extensively participates in nutrient cycling, heavy metal adsorption, and mineral redox transformation.[5−7] Naturally occurring and laboratory-synthesized hematite can have various morphologies (e.g., plates, needles, spindles, and pseudocubes) due to the incorporation of impurities (e.g., aluminum), the change of aging time, and the utilization of organic additives (e.g., citrate, maltose, amines, and dioxane) during the formation and transformation,[8] which gives the hematite different reactivities for the immobilization of heavy metals, for example, for arsenate.[9,10] In addition, a perfectly crystalline structure of hematite rarely exists in natural environments because of the biological corrosion of mineral surface and relatively low environmental temperature, thereby contributing to the generation of vacancy defects.[11−13] Therefore, vacancy defects, along with morphology, influence the physical and chemical properties of naturally occurring iron minerals.

Generally, defects in iron minerals arise from deviations in its perfect crystal structure, which typically include vacancies involving iron (Fe) and oxygen (O). Similar to the morphology, vacancy defects are also observed to have a considerable influence on the reactivity of Fe-bearing minerals. For example, vacancy defects were observed to trigger the electron transfer behavior of Fe(II)-goethite and accelerate the microbial reduction of goethite.[14,15] Iron minerals with attached fungi could generate more oxygen defects through fungal activity, thus indirectly modulating the peroxidase-like activity.[16] In addition, in our previous work, we confirmed that iron and oxygen vacancies could significantly promote the adsorption capacities of iron (oxyhydr)oxides for arsenate

Received: October 20, 2024
Revised: January 18, 2025
Accepted: January 21, 2025
Published: January 31, 2025

https://doi.org/10.1021/acs.est.4c11344
Environ. Sci. Technol. 2025, 59, 2802−2814

removal, which was attributed to the increase of As−Fe binding strength in the defect sites.[10,17] These findings indicate that vacancy defects are as crucial as the morphology in regulating the interfacial reaction behaviors of iron minerals. However, the surface terminations of hematite vary depending on its morphology.[6,18−21] For example, nanoplate-like hematite predominantly exposes the (001) facet, featuring doubly coordinated oxygen atoms in its surface termination.[22,23] In contrast, nanocube-like hematite, which exposes the (012) lattice facet, includes additional singly and triply coordinated oxygen atoms.[23,24] Liang et al. proposed that each Fe vacancy defect in the (001) facet of hematite could generate three $\equiv FeOH^{-0.5}$ and $\equiv Fe_3O^{-0.5}$ sites in the surface termination.[13] Notably, such defects have no obvious contribution to the increase in total site densities in the (012) facet of hematite because it has a rough surface characterized by "ridges" and "valleys" of oxygen atoms. This means that the sites on the surface termination of hematite, modified by vacancy defects, differ in their ability to adsorb heavy metals.

An increasing number of researchers have highlighted that the formation of vacancy defects in iron minerals can be triggered through both biotic and abiotic pathways in natural environments. For example, Hu et al. found that dissimilatory iron-reducing bacteria (DIRB), such as *Shewanella putrefaciens* CN-32, could induce the formation of vacancy defects on hematite surfaces through biological corrosion of the mineral surface.[25,26] Similar phenomena have also been observed with other microorganisms, such as the bacteria *Escherichia coli*[27] and the fungus *Talaromyces guizhouense* NJAU 4742.[16] Compared with biotic pathways, the incorporation of secondary metal ions represents a typical abiotic approach to generate vacancy defects in iron minerals. For instance, the substitution of structural Fe atoms by metal ions such as aluminum (Al), copper (Cu), and cobalt (Co) has been observed to create more vacancy defects in iron minerals.[28−30] This is largely due to the similar ionic radii of these metal ions to that of Fe, making isomorphous substitution a common phenomenon.[31] In addition to metal ion substitution, mineral crystal growth under low-temperature conditions is another abiotic approach that favors the formation of vacancy defects. Previous studies have demonstrated that manganese oxides formed at relatively low temperatures (e.g., 50 °C) exhibit more vacancy defects compared to those formed at higher temperatures (e.g., 120 or 180 °C).[32] Similarly, positron annihilation lifetime (PAL) spectroscopy has confirmed that poorly crystalline ferrihydrite prepared at room temperature exhibits larger vacancy defects than well-crystalline hematite prepared at 180 °C.[33] Therefore, vacancy defects are intrinsic characteristics of naturally occurring iron minerals. Moreover, the morphologies of iron minerals in natural environments can be influenced by isomorphous substitution and reaction temperature.[8] For instance, Al substitution is prevalent in tropical and subtropical soils, with the Al content in iron minerals (e.g., hematite) ranging between 7.7 and 11.3%.[34] The morphology of hematite is significantly affected by varying levels of Al substitution.[9,19] Common morphologies, such as cube-, plate-, and rod-like structures, are observed in hematite, each exposing distinct lattice facets.[9,21,35,36] These findings suggest that vacancy defects, driven by factors such as low temperatures, the prevalence of isomorphous substitution, and biological corrosion, are most likely to form on the various exposed lattice facets of morphology-dependent hematite in natural environments.

Fe-bearing minerals have been reported to act as a sink for arsenic, controlling its migration and fate in natural environments.[37,38] Additionally, Fe-bearing minerals are extensively employed as adsorbent materials for the remediation of arsenic-polluted soil and groundwater.[39−41] Although vacancy defects are intrinsic characteristics of hematite, it is still unclear how and why vacancy defects affect arsenic immobilization by morphology-dependent hematite. Revealing the quantitative contributions of vacancy defects to arsenic immobilization across various exposed facets of morphology-dependent hematite is therefore of scientific significance. It enhances our ability to predict the fate of toxic arsenic controlled by iron minerals in soils and sediments while providing a potential practical application for designing efficient remediation strategies to address As pollution. Herein, perfectly crystalline hematite samples with nanocube-, nanoplate-, and nanorod-like morphologies were treated with $NaBH_4$ to induce the formation of oxygen vacancies in their respective exposed lattice facets. The characteristics and contents of vacancy defects were carefully investigated using electron paramagnetic resonance (EPR),[42] positron annihilation lifetime spectrometry (PAL),[43,44] extended X-ray absorption fine spectroscopy (EXAFS),[45,46] and thermogravimetric analysis (TGA).[10] The objectives of this study are (1) to reveal the characteristics of vacancy defects in morphology-dependent hematite samples, (2) to evaluate the quantitative contribution of vacancy defects on arsenate immobilization across various lattice facets of hematite, and (3) to provide mechanistic insights into how vacancy defects on various lattice facets influence arsenate adsorption by hematite.

2. MATERIALS AND METHODS

2.1. Mineral Preparation. Perfectly crystalline hematite samples with nanoplate (denoted as HNP), nanocube (denoted as HNC), and nanorod (denoted as HNR) morphologies were synthesized according to procedures reported in the literature.[6,47,48] To produce vacancy defects in morphology-dependent hematite, we utilized $NaBH_4$ solutions to treat the perfectly crystalline hematite samples.[10,49] 0.32 g portion of hematite powder was added into $NaBH_4$ solutions (40 mL, 1 M concentration) at room temperature under magnetic stirring. After 2 h, the samples were thoroughly washed with deionized water and ethanol multiple times to eliminate any residual $NaBH_4$ adhering to the mineral surface and subsequently dried in an oven at 40 °C. The defective HNP, HNC, and HNR samples obtained were denoted as DHNP, DHNC, and DHNR, respectively. Details of preparation procedures for the hematite samples are presented in Text S1.

2.2. Bulk Characterizations. The mineral phase, morphology, and structure of the morphology-dependent hematite samples were characterized by using X-ray diffraction (XRD), scanning electron microscopy (SEM), transmission electron microscopy, synchrotron-based X-ray absorption spectroscopy (XAS), and X-ray photoelectron spectroscopy (XPS), respectively. The specific surface area was characterized by Brunauer−Emmett−Teller (BET) analysis. The defective structure of the hematite was characterized using electron paramagnetic resonance (EPR), angle-resolved X-ray photoelectron spectroscopy (ARXPS), and positron annihilation lifetime (PAL) spectroscopy. The surface-active sites, surface complex, and bonding analysis of As(V) on hematite were characterized by in situ diffuse reflectance infrared Fourier

https://doi.org/10.1021/acs.est.4c11344
Environ. Sci. Technol. 2025, 59, 2802−2814

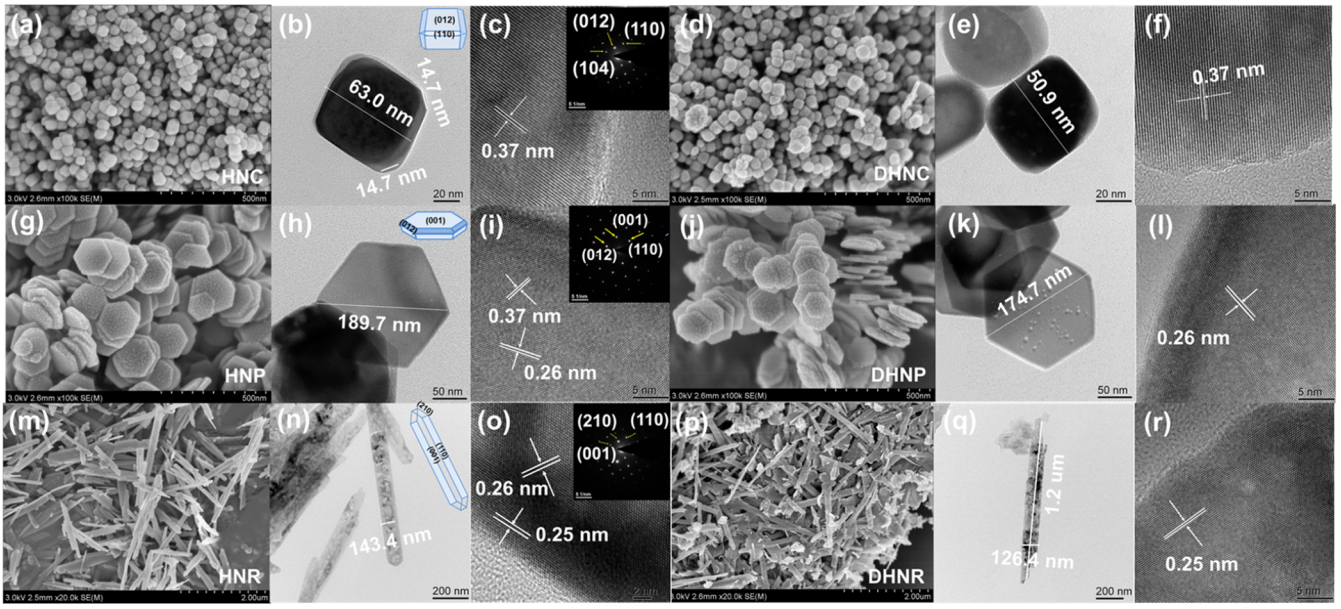

Figure 1. SEM (a, d, g, j, m, p), TEM (b, e, h, k, n, q), and HRTEM (c, f, i, l, o, r) images and the corresponding selected-area electron diffraction (SAED) (insets in c, i, o) of morphology-dependent hematite samples before and after $NaBH_4$ treatment.

transform spectroscopy (DRIFTS) and density functional theory calculations (DFT), respectively. Detailed information is presented in Text S2.

2.3. Quantification of Vacancy Defect Concentration in Morphology-Dependent Hematite. The vacancy defect concentration in morphology-dependent hematite samples was quantitatively calculated using the thermogravimetric (TG) analysis approach reported in our previous study.[10] Before the experiment, the samples were dried in the oven at 105 °C for 12 h to eliminate the effect of physical adsorption water on the OVD concentration measurements. First, a relatively slow heating rate of 0.5 °C min^{-1} was used for 30 min to purge the pipe further to obtain a relatively smooth baseline. Then, a certain mass of hematite samples was placed in a Pt crucible, and the curve was recorded from 45 to 850 °C in a flow of 5 vol % of the O_2/Ar with a heating rate of 10 °C min^{-1}.

2.4. Batch Arsenate Adsorption Experiments. Batch adsorption experiments were conducted at a stirring velocity of 280 rpm at 25 °C with an ionic strength of 0.02 M $NaNO_3$. Disodium arsenate heptahydrate ($Na_2HAsO_4{\cdot}7H_2O$) was prepared as the As(V) stock solution, and the initial stock concentrations of As(V) ranged from 0 to 0.27 mM. Hematite suspensions with initial concentrations of 0.15 g L^{-1} were prepared and stirred on a magnetic mixer for 24 h. The solution pH was adjusted to 6.0 by using 1 M HCl and 1 M NaOH. After 24 h, the supernatant was filtered through a membrane filter with a pore size of 0.22 μm. The concentrations of arsenate in the filtrates were measured by using an atomic fluorescence spectrometer (AFS-9700). To verify whether any As(III) species were formed via interactions with hematite during the batch experiments, we collected As K-edge XANES data of As(V) adsorbed hematite powders (Figure S1). Linear combination fitting results confirmed that only As(V) species were present on the surface of all hematite samples (Table S1), indicating that As(V) was not reduced to As(III) during the batch experiments.

2.5. Density Functional Theory (DFT) Calculations. DFT calculations were conducted to further explore the chemical behavior of the $H_2AsO_4^-$ ion on the (001), (012), and (110) surfaces of α-Fe_2O_3. All calculations were performed using the Vienna Ab initio Simulation Package (VASP) with the Perdew, Burke, and Enzerhof (PBE) formulation.[50,51] Projected augmented wave (PAW) potentials were applied to describe the ionic cores and account for valence electrons, utilizing a plane wave basis set with a kinetic energy cutoff of 450 eV.[52−54] The density of states (DOS) and crystal orbital Hamilton population (COHP) methods were utilized to analyze the bonding chemistry of surface complexes.[55,56] Details of the calculation parameters are presented in Text S3.

3. RESULTS AND DISCUSSION

3.1. Bulk Characterization. Figure S2a presents the XRD patterns of the synthesized hematite samples before and after treatment with $NaBH_4$ solutions. All diffraction signals of hematite samples were consistent with the crystallographic database (JCPDS 33-0664), indicating that HNP, HNC, and HNR samples exhibit the pure phase of hematite (α-Fe_2O_3). The sharp diffraction signals observed in the three hematite samples indicate their excellent crystallinity. The superior crystallinity of the hematite samples reflects a well-ordered periodic arrangement of Fe and O atoms in the structure, resulting in fewer atomic vacancy defects. After treatment using $NaBH_4$ solutions, the XRD patterns of DHNP, DHNC, and DHNR samples remained the same as before, and no new reflections corresponding to other iron minerals (e.g., goethite and/or magnetite) were observed in the patterns, indicating that the $NaBH_4$ treatment did not change the hematite structure. Boron (B) and sodium (Na) can be characterized by B 1s and Na 1s peaks in XPS spectra, which are commonly observed at binding energies of approximately 192 and 1071 eV, respectively. As shown in Figure S2b, the elements B and Na were neither detected in the $NaBH_4$-treated hematite samples using inductively coupled plasma optical emission spectrometry analysis (ICP-OES, 5110VDV, Agilent) nor were B 1s and Na 1s signals observed in the full XPS spectra, suggesting that Na and B were not incorporated into the hematite structure. The specific surface areas (SSA) of the

https://doi.org/10.1021/acs.est.4c11344
Environ. Sci. Technol. 2025, 59, 2802−2814

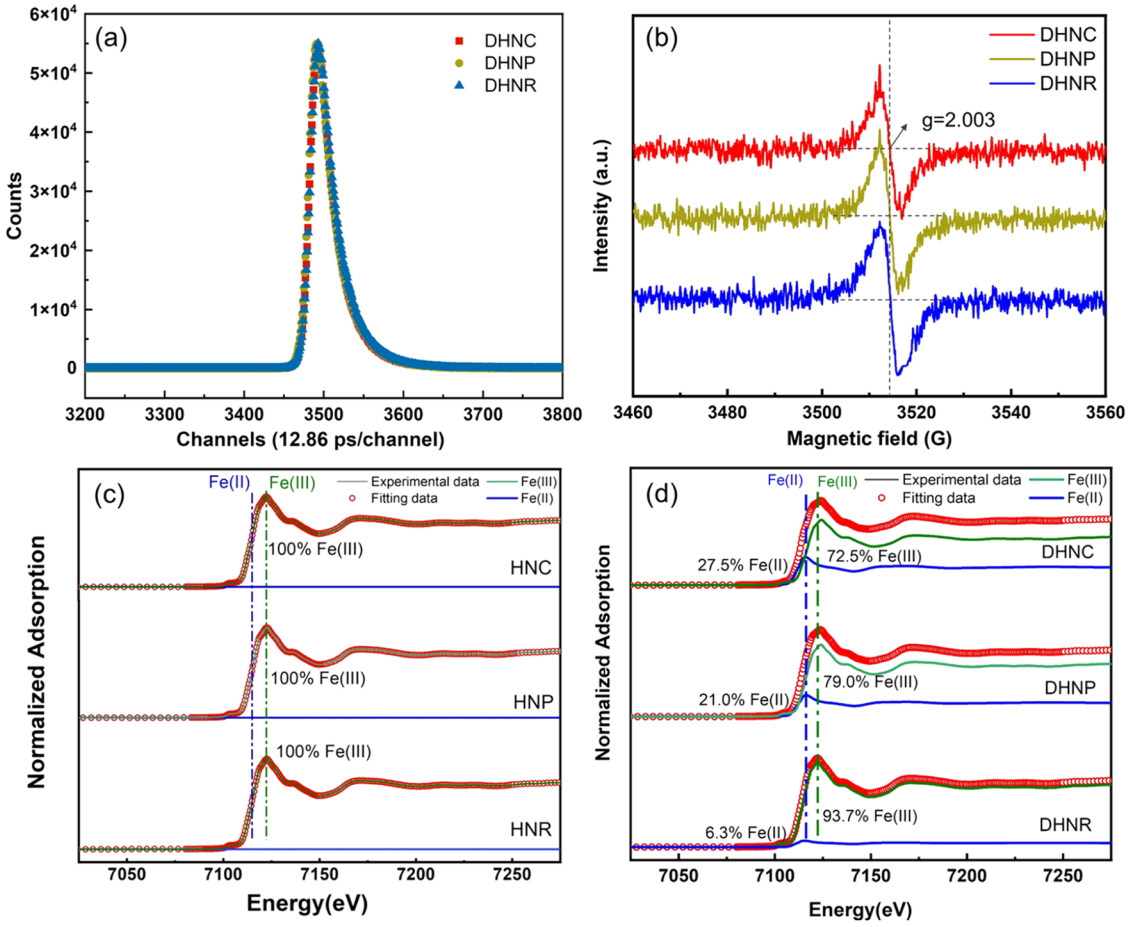

Figure 2. Positron annihilation lifetime spectra (a), EPR spectra (b), and Fe K-edge XANES spectra (c, d) of hematite samples.

hematite samples HNC, HNP, and HNR, as determined by the BET model, were 21.6, 22.5, and 40.0 $m^2\ g^{-1}$, respectively. Following the $NaBH_4$ treatment, the corresponding SSAs of the hematite samples increased to 42.7, 23.0, and 75.9 $m^2\ g^{-1}$, respectively.

To examine the evolution of the morphology of as-synthesized hematite samples before and after $NaBH_4$ treatment, we collected the SEM, TEM, and HRTEM images. As shown in Figure 1, the HNC sample exhibited nanocube-like morphology with average side lengths of 63.0 ± 9.7 nm. HRTEM revealed that HNC particles had the primary exposed facet of (012) with a lattice spacing of 0.37 nm. Notably, an easily overlooked (110) facet existing at the edge of the HNC particles was also observed in the selected area electron diffraction (SAED) patterns. The percentage fraction of each exposed facet in the hematite samples was determined based on the analysis of HRTEM and TEM images. The detailed calculation steps are provided in Text S4. The calculated percentage fraction of (012) and (110) facets in the HNC sample was ca. 72.8 and 27.2%, respectively, which was close to the values reported in previous work.[48] For the HNP sample, we observed a well-shaped hexagonal nanoplate morphology with average diameters of 189.7 ± 14.9 nm and thicknesses of 27.5 ± 4.5 nm. HRTEM images and SAED patterns revealed two lattice spacings of 0.37 and 0.26 nm in the HNP particles, which were attributed to the (001) and (012) facets, respectively. HNP particles consisted of ca.70.3% (001) and 29.7% (012) facets (Text S4), indicating that (001) was the primary exposed lattice facet in the HNP sample. In addition, the HNR sample was characterized by the nanorod-like morphology with average lengths of 1.8 ± 0.1 μm and widths of 143.4 ± 1.3 nm. Two main lattice spacings of 0.25 and 0.26 nm were observed in the HRTEM image of the HNR sample, which were assigned to the (110) and (001) facets. We also observed the (210) facet that existed in the HNR sample, as evidenced by the SAED patterns. However, the fraction of the (210) facet (4.4%), calculated from the SEM and TEM images, was far lower than those of (001) (48.3%) and (110) (47.3%) (Text S4), suggesting that the (110) and (001) facets were the primary exposed lattice facets in HNR samples. Remarkably, the $NaBH_4$ treatment did not alter the morphologies and primarily exposed lattice facets of HNC, HNP, and HNR (Figure 1d,j,p), but their sizes were noticeably reduced. For the DHNC sample, its average side lengths decreased to 50.9 nm, while the diameters for DHNP and widths for DHNR particles decreased to 174.7 and 126.4 nm, respectively. This result indicates that the $NaBH_4$ treatment reduced the particle size of hematite samples through reduction-induced erosion of the mineral surface, which was in agreement with the Rietveld structural refinement of their corresponding XRD patterns (Table S2). The small particle size leads to an increase in the specific surface areas of hematite, which explains why the three hematite samples exhibited relatively large specific surface areas after the $NaBH_4$ treatment. In addition, we observed that the extent to which $NaBH_4$ treatment affects particle sizes varies among the samples. This variation was attributed to the differing strengths of Fe−O bonds in the various exposed facets of hematite,[53] leading to significant differences in the

https://doi.org/10.1021/acs.est.4c11344
Environ. Sci. Technol. 2025, 59, 2802−2814

reduction-induced erosion susceptibility of hematite samples. Consequently, notable differences in the degree of the SSA increase were observed among the samples.

3.2. Vacancy Defect Characteristics in Morphology-Dependent Hematite. Positron annihilation lifetime (PAL) spectrometry is an effective and highly sensitive technique for identifying the type and size of atomic defects in minerals.[57] To illustrate the defect type in the morphology-dependent hematite samples, we collected PAL spectra of our DHNC, DHNP, and DHNR samples. The peak-normalized PAL profiles of three samples and the corresponding parameters are shown in Figure 2a and Table 1, respectively. The PAL spectra of hematite samples could be well decomposed into three distinct components: τ_1, τ_2, and τ_3. The shortest component (τ_1, 209−222 ps) was generally attributed to the free annihilation of positrons in the defect-free crystal. The longest one (τ_3, 1747−2152 ps) was due to the annihilation of orthopositronium atoms formed in the large voids present in the material. The medium lifetime component (τ_2, 389.5−406.3 ps) was assigned to the positrons captured by large defects in the minerals, such as oxygen vacancy defect clusters.[10,33] Therefore, the τ_2 component and its corresponding intensity (I_2) reflect the occurrence of oxygen vacancy defects in the hematite structure. As shown in Table 1, the intensity of the τ_2 component for the three hematite samples was the largest among the three components, indicating that the $NaBH_4$ treatment successfully generated oxygen vacancy defects in hematite. The formation of oxygen vacancies in hematite treated by $NaBH_4$ can be attributed to the strong reducing ability of the dissolved BH_4^- ion, which acts as an oxygen scavenger to rapidly remove surface oxygen atoms in the structure of hematite at room temperature. In this case, the surface electronic state of defective hematite differs significantly from that of defect-free hematite. The presence of oxygen vacancies increased the number of unpaired electrons in defective hematite, imparting paramagnetic properties. This characteristic could be effectively detected using electron paramagnetic resonance (EPR) spectroscopy, a widely employed method for analyzing oxygen vacancy defects.[58,59] As shown in Figure 2b, a noticeable signal at g = 2.003 was observed in the DHNC, DHNP, and DHNR samples, which was attributed to the electrons trapped in the oxygen defect sites.[60] In addition, when the oxygen atom of Fe_2O_3 is missing to form an oxygen vacancy, the Fe oxidation state of hematite will be reduced to maintain charge balance.[11,61] This reaction could be described as follows:

Table 1. Positron Annihilation Lifetime Parameters of Defective Fe_2O_3 Samples

samples	τ_1 (ps)	I_1 (%)	τ_2 (ps)	I_2 (%)	τ_3 (ns)	I_3 (%)
DHNC	197.50	37.10	362.00	62.00	2.19	0.90
DHNP	203.00	28.40	353.90	70.70	2.28	0.90
DHNR	251.00	46.40	386.00	52.70	2.44	0.89

$$Fe_2O_3 \rightarrow Fe_y^{2+}Fe_{2-y}^{3+}O_{3-x}^{2-} + \frac{x}{2}O_2 \quad (1)$$

where x and y represent the oxygen vacancy content and the fraction of Fe^{2+} species in α-Fe_2O_3 samples, respectively. Therefore, we investigated the evolution of the Fe oxidation state of morphology-dependent hematite samples before and after $NaBH_4$ treatment through linear combination fitting (LCF) of their corresponding Fe K-edge XANES spectra (Figure 2c,d and Table S3). LCF results revealed that only Fe(III) species were observed in the HNC, HNP, and HNR samples (Figure 2c). In general, perfect hematite (α-Fe_2O_3) exhibits a theoretical chemical valence of +3. The predominant Fe(III) oxidation state observed in the HNC, HNP, and HNR samples suggests that these samples closely resemble the defect-free hematite structure. Interestingly, both Fe(II) and Fe(III) species appeared in the hematite samples after $NaBH_4$ treatment, indicating that $NaBH_4$ treatment reduced the oxidation state of Fe in hematite. Since the $NaBH_4$ treatment did not alter the phase structure of the three hematite samples (Figure S2), the decrease in the Fe oxidation state observed in the DHNC, DHNP, and DHNR samples could be attributed to the formation of oxygen vacancies, helping maintain charge balance, as described in eq 1. However, the fraction of Fe(II) (27.5%) in the DHNC sample was obviously larger than that in the DHNP (17.7%) and DHNR (6.3%) samples (Figure 2d). This result indicated that the DHNC sample generated the highest oxygen vacancy defect concentration by $NaBH_4$ treatment, followed by DHNP and DHNR samples.

To illustrate the possible existence of oxygen vacancies on the surface or in the bulk of defective hematite samples, angle-resolved X-ray photoelectron spectroscopy (ARXPS) data of defective hematite samples were collected to analyze the evolution of the Fe and O oxidation states at surface depths of ∼3.5 and ∼10 nm, respectively (Figures S3 and S4). The corresponding fitting parameters are shown in Tables S4 and S5. The Fe^{2+}/Fe^{3+} molar ratios in the DHNC, DHNP, and DHNR samples, calculated by fitting their corresponding Fe 2p XPS spectra at a surface depth of ∼10 nm, were 1.35, 2.23, and 1.20, respectively. The relatively higher Fe^{2+}/Fe^{3+} molar ratio in the DHNP samples compared to that in DHNC and DHPR further confirmed that the DHNP sample had more oxygen vacancy defects than the DHNC and DHPR samples. Remarkably, the Fe^{2+}/Fe^{3+} molar ratios in the DHNC, DHNP, and DHNR samples at a surface depth of ∼3.5 nm decreased to 1.49, 3.31, and 1.28, respectively, indicating that Fe^{2+} species in hematite primarily gathered on the shallow surface after $NaBH_4$ treatment. The relatively higher Fe^{2+} species on the shallow surface of defective hematite revealed that oxygen vacancies were mainly located at the surface rather than in the bulk. This was because the oxygen atoms in the subsurface or bulk of hematite were less accessible for direct interaction with the $NaBH_4$ solution. In contrast, the $NaBH_4$ solution preferentially reacted with the oxygen atoms on the hematite surface, resulting in the formation of oxygen vacancies on the surface structure of defective hematite.

As the calculation of oxygen vacancies from the fitting results of XPS and XAS spectra is an indirect approach, it inevitably introduces fitting errors due to the use of varying input parameters. To accurately quantify the OVD concentration in morphology-dependent hematite samples, thermogravimetric analysis (TGA) was employed in this study because it has been confirmed to be a suitable method for quantifying the OVD concentration compared to XPS and XAS analysis.[10] The TG profiles recorded an increase in weight for the DHNC, DHNP, and DHNR samples at temperatures ranging from 300 to 600 °C in a 5% O_2/Ar atmosphere. This weight gain was attributed to the incorporation of oxygen molecules into the oxygen vacancies in hematite at such elevated reaction temperatures.[62] Remarkably, the weight of HNC, HNP, and HNR samples did not increase in a 5% O_2/Ar atmosphere (Figure S5). This

https://doi.org/10.1021/acs.est.4c11344
Environ. Sci. Technol. 2025, 59, 2802−2814

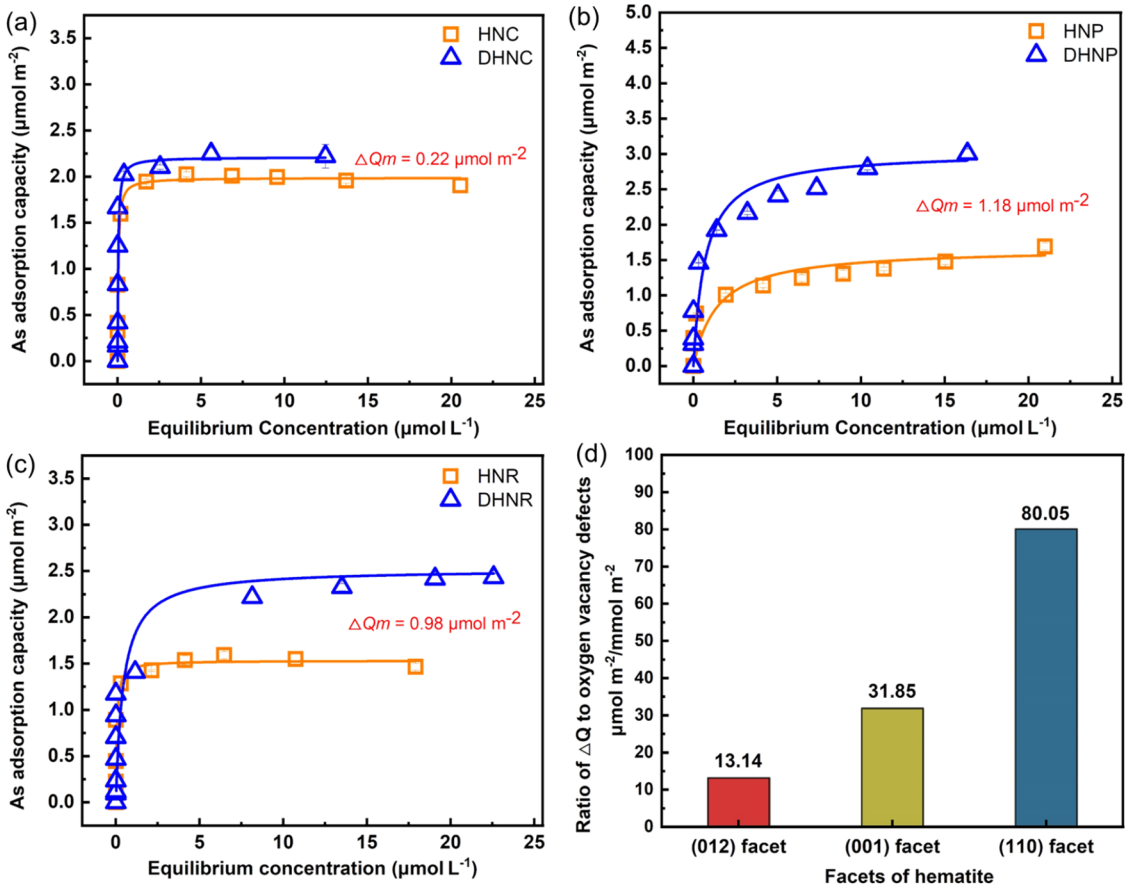

Figure 3. Arsenate adsorption isotherms fitted by the Langmuir equation (a–c) and the quantitative contribution of oxygen vacancies on (001), (110), and (012) exposed lattice facets of hematite samples to promoting the amount of As(V) adsorption (d).

result indicated that pristine HNC, HNP, and HNR samples had very few vacancies, which were hard to detect by TG analysis. The OVD concentration of DHNC, DHNP, and DHNR samples, calculated by the weight change, were 1.36, 1.59, and 0.98 mmol g^{-1}, respectively (Table S6), suggesting that the DHNP sample had the largest OVD concentration among them under the same treatment of $NaBH_4$ concentration.

3.3. Quantitative Contribution of Oxygen Vacancies on Various Exposed Facets to Promoting Arsenate Immobilization. To investigate As(V) adsorption on morphology-dependent hematite samples, macroscopic batch adsorption experiments were performed at pH 6.0 (Figure 3). The maximum As(V) adsorption capacities of hematite samples were evaluated by fitting their corresponding isotherm adsorption curves using the Langmuir model (Figure 3 and Table S7). The maximum adsorption capacities of HNC, HNP, and HNR samples for As(V) removal were 61.27, 42.86, and 37.93 μmol g^{-1}, respectively. To consider the differences in specific surface area (SSA) for the different hematite samples for arsenate immobilization, the maximum As(V) adsorption capacities of morphology-dependent hematite samples were normalized by their SSA values (Figure 3). This calculation revealed that the maximum As(V) adsorption amount per unit surface area was highest for the HNC sample (1.99 μmol m^{-2}), followed by HNP (1.68 μmol m^{-2}) and HNR (1.53 μmol m^{-2}). This phenomenon was also observed in previous work and was attributed to the varying exposed lattice facets in morphology-dependent hematite samples, leading to different bonding strengths of As(V) on the hematite surface.[38,48] Interestingly, the As(V) adsorption capacities of morphology-dependent hematite samples increased after $NaBH_4$ treatment, suggesting that the formation of oxygen vacancies in the surface structure of hematite enhanced the As(V) adsorption. Nevertheless, the OVDs exhibited a different degree of influence on the enhancement of As(V) adsorption by morphology-dependent hematite samples. The maximum amounts of As(V) adsorbed per unit surface area of DHNC, DHNP, and DHNR samples were 2.21, 2.86, and 2.51 μmol m^{-2}, respectively. The increased amplitude of As(V) adsorption amount (ΔQ_m, mmol m^{-2}) on DHNC, DHNP, and DHNR was 0.22, 1.18, and 0.98 μmol m^{-2}, respectively. In this case, the DHNR sample had the lowest OVD concentration, its enhanced As(V) adsorption amount per unit OVD concentration (ΔQ_{def}, μmol/$mmol_{def}$), however, was the largest one, which was 6.1 and 2.5 times larger than those of the DHNC and DHNP samples, respectively. This result indicated that the OVDs had the largest contribution to improving As(V) immobilization on the HNR sample.

HNP and HNC samples showed the primarily exposed facets of (001) and (012), respectively, while the primarily exposed facets for HNR were (001) and (110). We therefore calculated the enhanced As(V) sorption induced by OVDs on the (001), (012), and (110) exposed facets of hematite based on the OVD concentration calculated by TG analysis, the proportion of exposed lattice facets lattice obtained from TEM analysis, and the As(V) adsorption amount of hematite

https://doi.org/10.1021/acs.est.4c11344
Environ. Sci. Technol. 2025, 59, 2802–2814

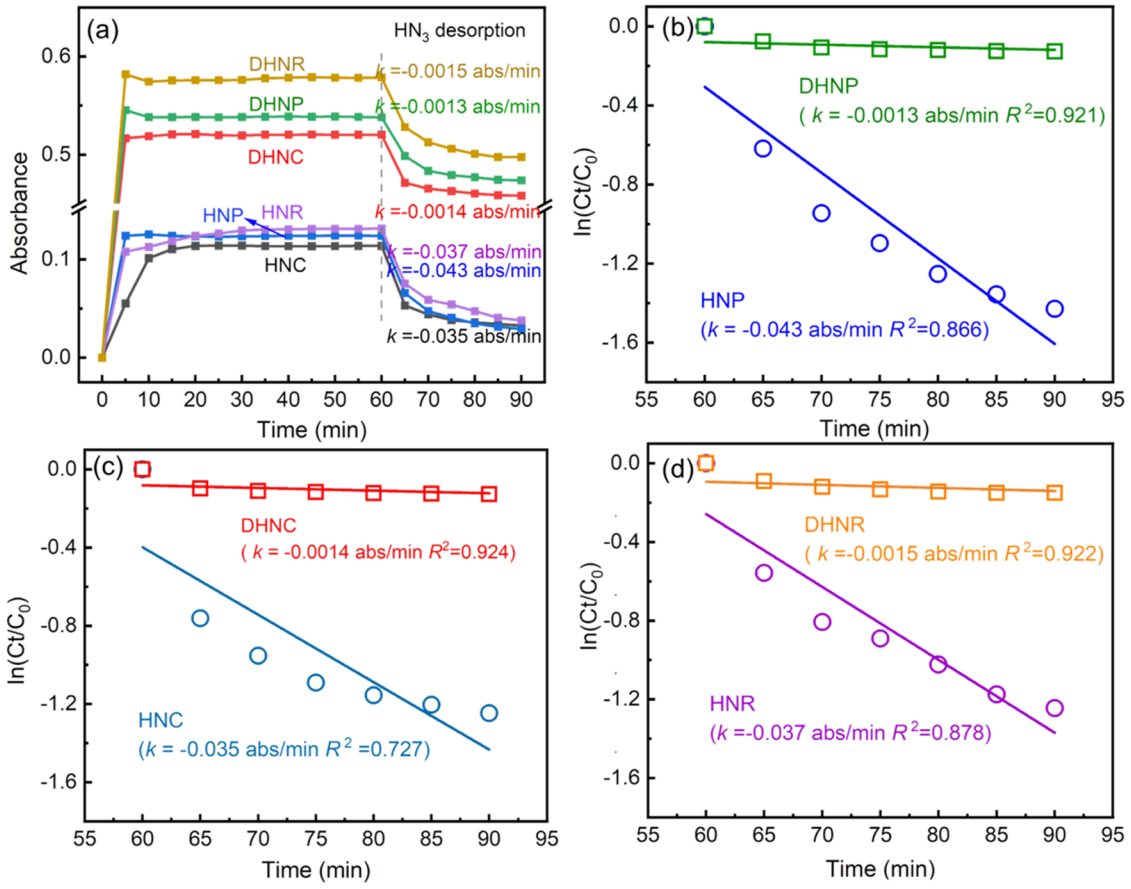

Figure 4. Evolution of the peak intensity at ~1620 cm^{-1} from the DRIFT spectra for NH_3 adsorption/desorption (a) and pseudo-first-order kinetics model for fitting NH_3 desorption on morphology-dependent hematite samples (b–d).

samples. The details of these calculation procedures are listed in Text S5. The calculation results showed that the enhanced As(V) adsorption amount per unit oxygen concentration on the (012), (001), and (110) facets was 13.14, 31.85, and 80.05 $\mu mol/mmol_{def}$, i.e., increasing 1 mmol OVD concentration on the (012), (110), and (001) facets of hematite could improve the As(V) adsorption amount by 13.14, 80.05, and 31.85 μmol, respectively (Figure 3d). This result indicated that the contribution of OVDs on the (110) facet to the enhancement of As(V) immobilization by hematite was far larger than those on the (012) and (001) facets.

3.4. Evolution of Surface-Active Sites on Defect-Free and Defective Hematite with Different Morphologies. Although we have demonstrated the different extents of the effect of OVDs on As(V) immobilization by hematite with different morphologies, it was still unclear why the contribution of OVDs in nanorod-like hematite was larger than those in nanocube-like and nanoplate-like hematite samples. In this study, we collected *in situ* NH_3-DRIFT spectra of different hematite samples to follow the evolution of surface-active sites in defective hematite samples (Figures S6 and S7). The DRIFT spectra displayed two distinct infrared (IR) characteristic peaks at approximately 1628 and 3330 cm^{-1} after adsorbing NH_3 for 60 min (Figure S6), suggesting strong adsorption of NH_3 on all hematite samples. The peaks at ~1620 and ~3330 cm^{-1} were assigned to symmetric deformation of NH_3 bound to Lewis acid sites, while those at ~1440 cm^{-1} and in the range of 1850–1640 cm^{-1} were ascribed to NH_3 bound to Brønsted acid sites.[63−65] Remarkably, no characteristic bands at ~1440 cm^{-1} and in the range of 1850–1640 cm^{-1} were observed in the DRIFT spectra of all samples, indicating that the Lewis acid sites, but not Brønsted acid sites, were involved as active sites for As(V) immobilization by hematite. As the uncoordinated Fe atoms on the hematite surface were defined as the Lewis acid sites in previous work,[53] our data suggest that the formation of OVDs induced by $NaBH_4$ treatment was accompanied by the production of more uncoordinated Fe atoms, thus generating more Lewis acid sites for As(V) immobilization.

The bonding strength of surface complexes is associated with the strength of the Lewis acid sites. We therefore followed NH_3 desorption behavior on defective hematite samples through subsequent Ar purging (Figure S7). The IR characteristic peak at ~1620 cm^{-1} gradually disappeared, suggesting the adsorbed NH_3 was gradually desorbed from the surface of hematite samples. NH_3 desorption kinetic behavior on different samples was investigated using a pseudo-first-order kinetic model based on the collected DRIFT spectra data. As shown in Figure 4, the calculated values of desorption rate constants (k) fitted by the pseudo-first-order kinetics model were −0.043, −0.035, and −0.037 abs min^{-1} for HNP, HNC, and HNR samples, respectively. The relatively larger absolute value of k for the HNP sample, compared to those for the HNC and HNR samples, indicates that the (001) facet has a weaker Lewis acid strength compared to the (110) and (012) facets, thereby leading to more rapid NH_3 desorption from the hematite surface. Interestingly, after $NaBH_4$ treatment, the absolute value of k for the hematite samples significantly

https://doi.org/10.1021/acs.est.4c11344
Environ. Sci. Technol. 2025, 59, 2802−2814

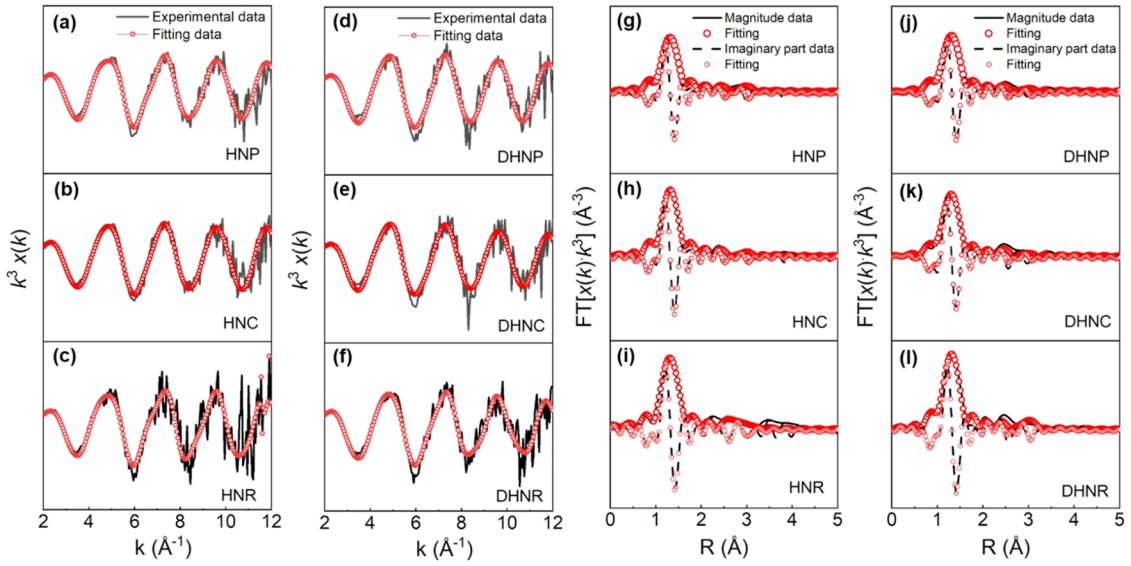

Figure 5. Fourier transformed *k* space (a–f) and *R* space curves of As–K-edge EXAFS spectra (g–l) on defect-free and defective hematite samples.

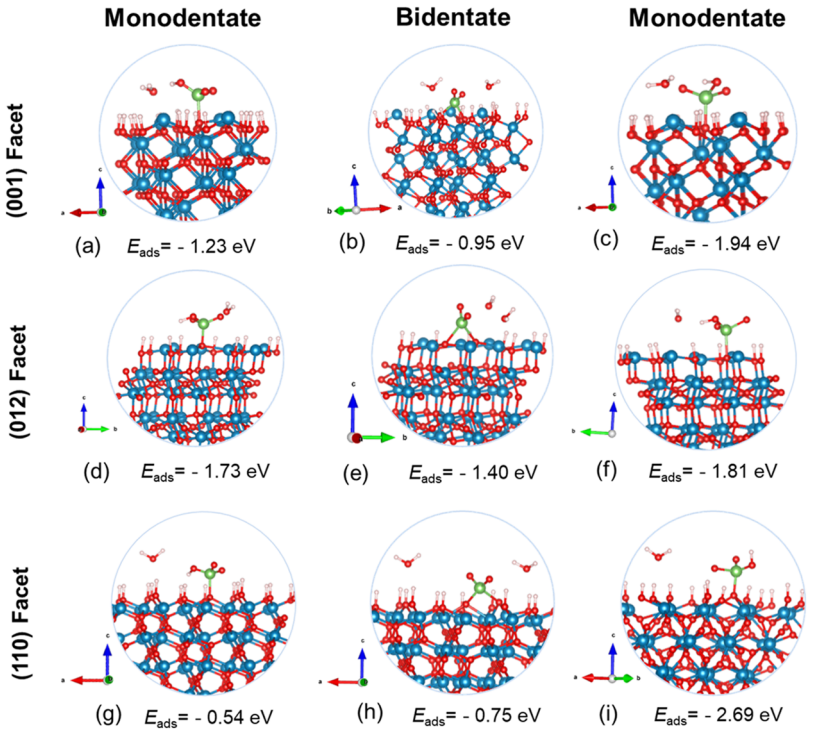

Figure 6. Optimized structure of inner-sphere As(V) ($H_2AsO_4^-$) monodentate and bidentate adsorption complexes on the (001), (012), and (110) facet of the defect-free (a, b, d, e, g, h) and defective hematite (c, f, i): white represents hydrogen atoms, green represents arsenic atoms, red represents oxygen atoms, and blue represents Fe atoms.

decreased, shifting to −0.0013, −0.0014, and −0.0015 abs min^{-1} for the DHNP, DHNC, and DHNR samples, respectively. This result suggests that the oxygen vacancies facilitated the formation of additional Lewis acid sites, which exhibited strong interactions with NH_3 molecules, thereby reducing the NH_3 desorption rate of hematite.

3.5. Local Coordination of As(V) Species Associated with Morphology-Dependent Hematite Surfaces. We collected As K-edge EXAFS spectra of As(V) adsorbed to the different hematite samples to observe the evolution of surface complexes of As(V) on defect-free and defective hematite surfaces. The Fourier transformed *k* space and *R* space curves of As K-edge EXAFS spectra are shown in Figure 5. Two shells of As–O and As–Fe were obviously observed in the FT EXAFS spectra of As(V)-adsorbed hematite samples. In the first As–O shell, the atomic distance (R_{As-O}) and the coordination number (N_{As-O}) for all samples were ∼1.70 Å and 4.0, respectively, which was assigned to an AsO_4 tetrahedron structure,[53] indicating that the oxidation state of As(V) adsorbed on hematite did not change. In the second Fe–As shell, the atomic distance (R_{As-Fe}) in the HNC and HNP sample was around 3.40 Å, suggesting the formation of a monodentate Fe–As complex on the hematite surface.[66−68] However, the R_{As-Fe} value in the HNR sample shifted to ∼3.31

https://doi.org/10.1021/acs.est.4c11344
Environ. Sci. Technol. 2025, 59, 2802−2814

Å. The relatively low R_{As-Fe} value in the HNR sample indicated an obviously different As−Fe complex compared to that in HNC and HNP samples. According to a previous study, the R_{As-Fe} value at ∼3.31 Å can be attributed to the formation of a bidentate binuclear As−Fe complex,[66] which was also confirmed by its coordination number (N_{Fe-As}) of 2 (Table S8). In addition to As−O and As−Fe shells, we also observed a commonly found As−O−O shell with an N_{As-O-O} of 12 and an R_{As-O-O} of 3.08−3.16 $Å^{-1}$ for all samples. This was attributed to the As−O−O multiple scattering in the structure of an AsO_4 tetrahedron.[53] Interestingly, the vacancy defects did not change the local coordination of As−Fe in the DHNC and DHNP samples. However, the R_{As-Fe} value in the DHNR sample shifted from 3.31 to 3.41 Å after $NaBH_4$ treatment, suggesting that monodentate Fe−As complexes are more likely to form than bidentate binuclear Fe−As complexes in defective hematite. This is because the surface of defective hematite contains an abundance of uncoordinated Fe atom sites, where oxyanion As(V) species can readily insert and directly bind to these sites, leading to the formation of monodentate Fe−As complexes. Previous studies have observed that the exposed lattice facets could influence the formation of As−Fe complexes due to the varied surface terminations of hematite.[53] In our study, we further revealed that vacancy defects also influence the formation of As−Fe complexes as they can modify the surface terminations of hematite.

3.6. Effect of Vacancy Defects on As(V) Adsorption to Different Exposed Facets of Hematite. In order to reveal the effect of OVDs on As(V) adsorption on different exposed facets of hematite particles, we carried out DFT calculations to investigate the reaction adsorption energy (E_{ads}) of arsenate on the hematite surface. The (001), (012), and (110) hematite slabs were constructed for DFT calculations as HNP, HNC, and HNR samples exhibited the predominately exposed lattice facets (001), (012), and (110), respectively. Figure S8 shows the surface atomic arrangements of the three hematite slabs. As shown in Figure S8, the (012) hematite slab was corrugated with alternating ridges of singly coordinated oxygen groups and valleys over triply coordinated oxygen groups running parallel to (121). However, the iron atom layers on the (110) and (001) hematite slabs were arranged neatly, which was obviously different from the (012) hematite slab. Figure 6 illustrates the optimized structures of inner-sphere As(V) ($H_2AsO_4^-$) adsorption on the (001), (012), and (110) hematite slabs in the absence and presence of one oxygen vacancy. In this study, we constructed two As−Fe complex models of monodentate and bidentate complexes to reveal the As(V) adsorption behavior on pristine hematite slabs. The calculated E_{ads} of As(V) on the (001) hematite slab in the form of the monodentate model was −1.23 eV, which was lower than that in the bidentate model (−0.95 eV) (Figure 6a,b). The adsorption behavior of As(V) on the (012) hematite slab showed the same tendency as observed on the (001) hematite slab, i.e., the calculated E_{ads} of As(V) in a monodentate configuration (−1.73 eV) was lower than that in a bidentate configuration (−1.40 eV) (Figure 6d,e). This result indicated that As(V) adsorption onto the (012) and (001) hematite slabs in a monodentate configuration was thermodynamically favorable, which explained the observation of monodentate As−Fe complexes in the HNP and HNC samples based on As K-edge EXAFS analysis. Remarkably, the calculated E_{ads} of As(V) on the (012) hematite slab in the form of the monodentate model (−0.54) was higher than that in the form of the bidentate model (−0.75 eV) (Figure 6g,h), indicating that the formation of an As−Fe monodentate complex on the (012) hematite slab was more favorable than that of an As−Fe bidentate complex, which was in agreement with the result of As K-edge EXAFS analysis for the HNR sample.

In addition, we observed that the E_{ads} of As(V) on the (012) hematite slab was lower than those on the (001) and (110) hematite slabs, suggesting that As(V) binds more strongly to the (012) facet than to the (001) and (110) facets of hematite. This explained why the As(V) adsorption amount per unit surface area was higher in the HNC sample than in the HNP and HNR samples (Figure 3). Although the exposed lattice facets of hematite had strong effects on the As(V) adsorption, it did not ignore the role of oxygen vacancies in promoting the affinity of the iron mineral to As(V). For the (012) hematite slab with one oxygen vacancy, its E_{ads} of As(V) in the monodentate model adjacent to the oxygen vacancy atom decreased from −1.73 to −1.84 eV, indicating that the presence of oxygen vacancy defects in the (012) facet improved As(V) adsorption on hematite. Compared to the defective (012) hematite slab, the E_{ads} of As(V) on the defective (001) hematite slab further decreased to −1.94 eV. Remarkably, the E_{ads} of As(V) on the defective (110) hematite slab considerably shifted from −0.75 to −2.69 eV. This result indicates that the oxygen vacancy defects enhanced the reactivity of the (110) facet, effectively activating it as a highly active facet for As(V) immobilization, while it has a relatively low influence on the highly active facet of (012). Therefore, the greater contribution of OVDs on the (110) facet, compared to the (012) and (001) facets, to promote As(V) immobilization could be attributed to the enhanced adsorption strength induced by oxygen vacancies.

3.7. Chemical Bonding Analysis of As(V) on Hematite With and Without Defects. Uncovering the evolution of the highest occupied molecular orbital (HOMO) and the lowest unoccupied molecular orbital (LUMO) of adsorbed species can provide in-depth mechanistic insights into the interfacial behavior of As on the hematite surface. To further reveal the effect of OVDs on As(V) immobilization, we performed a chemical bonding analysis to investigate the HOMO and LUMO of As(V) species adsorbed on different exposed facets of hematite. The DOS profile of the individual arsenate ion revealed that As and O atoms primarily occurred in LUMO and HOMO, respectively. We could observe an obvious localization of the electron density of As and O atoms in an individual arsenate ion, as evidenced by its narrow distribution of electron density (Figure S9). The electron densities of As and O atoms obviously overlapped after As(V) adsorption on a defect-free hematite slab, indicating that the electron density below the Fermi level was delocalized. Interestingly, the degree of electron delocalization for the LUMO and HOMO after As(V) adsorption on defective hematite slab was more pronounced than those on defect-free hematite, as evidenced by their relatively lower and broader intensity in the LUMO and HOMO of DOS profiles. The enhanced electron delocalization of As(V) adsorbed on defective hematite suggested that OVDs affected the chemical bonding of As(V) on the hematite surface, thereby facilitating the formation of stable As−O−Fe complexes. The crystal orbital Hamilton population (COHP) value is a quantitative measure of the bonding strength between atoms in a mineral, where a more negative COHP value indicates a stronger bond. To quantify the effect of oxygen vacancies on the chemical

https://doi.org/10.1021/acs.est.4c11344
Environ. Sci. Technol. 2025, 59, 2802−2814

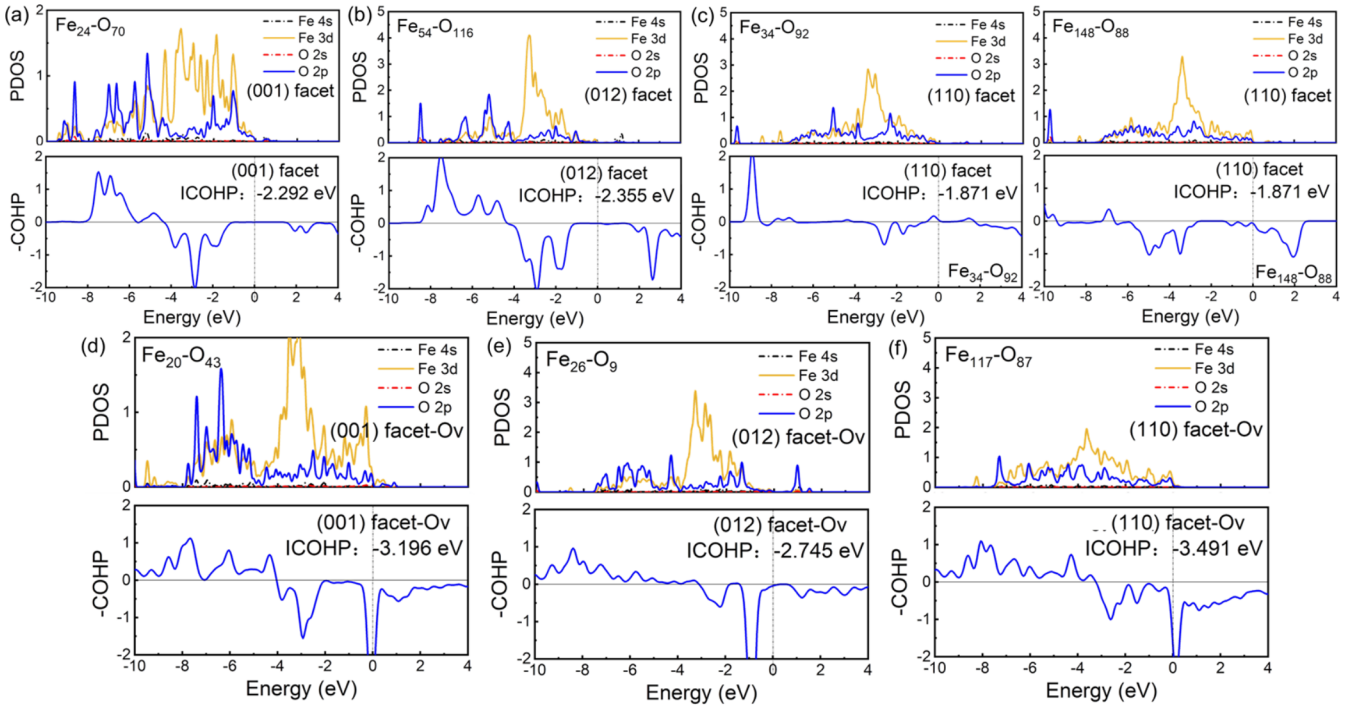

Figure 7. PDOS and −COHP plots of the Fe−O bonds in the As(V) complex on the defect-free (a−c) and defective hematite (d−f).

bonding strength of As(V) on different exposed lattice facets of hematite, the COHP value was calculated through analyzing their partial density of states (PDOS) profiles of Fe−O pairs (Figure 7 and Table S9). As shown in Figure 7, the bonding area below the Fermi level exhibited an obvious overlap for As-bound O 2p and Fe 3d atom orbitals, suggesting that the interaction between Fe 3d and O 2p contributes to the formation of new Fe−O bonds at the surface of hematite slabs. The electron delocalization for Fe and O atoms in different facets is different after As(V) adsorption, which was in agreement with the DOS analysis. The calculated COHP value for the coordinated Fe−O on the pristine (001) hematite slab was −2.292 eV, which was lower than that on the pristine (012) hematite slab (−2.355 eV). In addition, the COHP value for the two coordinated Fe−O bonds of $Fe_{34}O_{92}$ and $Fe_{148}O_{88}$ on the pristine (110) slab was −1.871 eV. Since the COPH value for the coordinated Fe−O on the pristine (012) hematite slab was more negative than those on the (001) and (110) hematite slabs, the bonding strength of As(V) on the pristine (012) slab was therefore the strongest among them, which agreed well with the result of our DFT calculations. The differences in the bonding strength of As(V) on various exposed facets of hematite were also reported in previous studies.[53] This was attributed to the intrinsic facet-dependent nature of hematite, characterized by the varying arrangements of Fe and O atoms on the surface terminations of different exposed facets, which introduced chemical diversity in the surface sites for As adsorption.[53] For the defective (001) and (012) slabs, their COHP values decreased to −3.196 and −2.745 eV, respectively, indicating that vacancy defects enhanced the bonding strength of As(V) on the (001) and (012) facets of hematite. However, the COPH value in the defective (001) hematite slab was more negative than that in the defective (012) hematite slab. Therefore, the surface sites of the (001) slab, modified by vacancy defects, exhibited greater activity for arsenic immobilization than those of the (012) facet. Notably, a significant increase in As(V) bonding strength was observed on the defective (110) slab, as evidenced by a substantial decrease in the COHP value to −3.419 eV. The lowest COPH value for coordinated Fe−O on the defective (110) hematite slab indicated that As(V) species exhibited the strongest adsorption on the defective (110) facet. Since the defect-free (110) facet of hematite showed the lowest affinity to As(V), the significant increase of the As(V) bonding strength on the surface of defective (110) facet suggested that oxygen vacancies made the largest contribution to promoting As(V) immobilization on the (110) facet, followed by the (001) and (110) facets, which was consistent with the result of reaction adsorption energy obtained from DFT calculations (Figure 3d). To sum up, the chemical diversity of surface-active sites on different exposed lattice facets of (001), (110), and (012) was responsible for the variations in As(V) adsorption. However, the presence of oxygen vacancy defects further altered the surface atom arrangement of Fe and O atoms and the local electronic structure of exposed facets, thereby influencing the HOMO and the LUMO of adsorbed As species (Figure 7a). Specifically, for the defective (110) facet, the lowest negative COHP value after As(V) adsorption indicates the highest level of electron delocalization. This substantial electron delocalization in the defective (110) facet facilitates the formation of more stable As−O−Fe complexes. This explained why we observed the largest enhancement of the As(V) adsorption capacity on the (110) facet induced by oxygen vacancies.

4. ENVIRONMENTAL IMPLICATIONS

In this study, morphology-dependent hematite samples with oxygen vacancy defects were synthesized through a $NaBH_4$ treatment. We carefully examined the vacancy defect characteristics in the hematite samples by using a series of advanced characterization techniques. PAL and XANES analyses demonstrated that oxygen vacancies were the primary defect

https://doi.org/10.1021/acs.est.4c11344
Environ. Sci. Technol. 2025, 59, 2802−2814

type present in the surface structure of hematite samples. For the first time, we revealed that oxygen vacancy defects in the hematite structure are as important as morphology, substantially affecting the interface reactivity for As(V) immobilization. Vacancy defects were observed to provide a greater enhancement for As(V) immobilization on the (110) facet of hematite compared to the (012) and (001) facets, effectively activating it as a highly active facet, as evidenced by DFT calculations and chemical bonding analysis. Hematite is one of the most abundant iron oxides in soils.[8] Given that Fe-bearing minerals are well-documented to act as sinks for arsenic, interfacial reactions between hematite and arsenic are most likely to occur within arsenic-polluted soil systems at the soil mineral-water interface, significantly influencing the migration and fate of arsenic. However, naturally occurring hematite often exhibits various morphologies and exposed lattice facets due to the incorporation of impurities (e.g., aluminum) at varying concentrations. These impurities, along with other abiotic factors such as temperature and redox conditions, as well as biotic factors like biological corrosion of mineral surface,[16,27,69] also contributed to the formation of defects, resulting from deviations in the perfect mineral structure. Therefore, both morphology and vacancy defects should be simultaneously considered when evaluating the migration and fate of As(V) controlled by iron minerals, as this approach more accurately reflects real environmental conditions. In addition, facet and vacancy defect engineering have been extensively applied to tailor the reactivities of mineral materials, enhancing their efficiency in removing pollutants.[70−73] Therefore, the integrated consideration of facets and vacancy defects provides valuable insights into optimizing the properties of iron-based materials, enabling improved performance in environmental remediation applications. The findings of this study not only aid in the development of highly efficient Fe-based mineral materials by tuning the vacancy defects in the structure for the remediation of As-polluted sites but also enhance a precise understanding of the migration and fate of toxic arsenic in polluted soil and sediments.

■ ASSOCIATED CONTENT

Supporting Information

The Supporting Information is available free of charge at https://pubs.acs.org/doi/10.1021/acs.est.4c11344.

The details of preparation procedures for all hematite samples; characterization of XRD, SEM, TEM, BET, XPS, ARXPS, EPR, PAL, DRIFT, XAS, and DFT calculation; calculations of percentage of the exposed facets in hematite samples; calculations of quantitative contribution of OVDs on the exposed lattice facets to promoting As(V) immobilization by hematite; and additional figures and tables as mentioned in this paper. (PDF)

■ AUTHOR INFORMATION

Corresponding Author

Jingtao Hou − *State Environmental Protection Key Laboratory of Soil Health and Green Remediation, Hubei Key Laboratory of Soil Environment and Pollution Remediation, College of Resources and Environment, Huazhong Agricultural University, Wuhan 430070, China;* orcid.org/0000-0002-2472-8309; Email: houjt87@163.com

Authors

Juan Liu − *State Environmental Protection Key Laboratory of Soil Health and Green Remediation, Hubei Key Laboratory of Soil Environment and Pollution Remediation, College of Resources and Environment, Huazhong Agricultural University, Wuhan 430070, China*

Juan Xiong − *State Environmental Protection Key Laboratory of Soil Health and Green Remediation, Hubei Key Laboratory of Soil Environment and Pollution Remediation, College of Resources and Environment, Huazhong Agricultural University, Wuhan 430070, China;* orcid.org/0000-0003-4414-536X

Lu Ren − *School of Civil Engineering, Suzhou University of Science and Technology, Suzhou 215009, China;* orcid.org/0000-0002-2166-1030

Mingxia Wang − *State Environmental Protection Key Laboratory of Soil Health and Green Remediation, Hubei Key Laboratory of Soil Environment and Pollution Remediation, College of Resources and Environment, Huazhong Agricultural University, Wuhan 430070, China;* orcid.org/0000-0002-5244-432X

Wenfeng Tan − *State Environmental Protection Key Laboratory of Soil Health and Green Remediation, Hubei Key Laboratory of Soil Environment and Pollution Remediation, College of Resources and Environment, Huazhong Agricultural University, Wuhan 430070, China*

Andreas Kappler − *Geomicrobiology, Department of Geosciences, University of Tübingen, Tübingen 72076, Germany;* orcid.org/0000-0002-3558-9500

Complete contact information is available at: https://pubs.acs.org/10.1021/acs.est.4c11344

Notes

The authors declare no competing financial interest.

■ ACKNOWLEDGMENTS

This work was supported by the National Natural Science Foundation of China (42277015, 42277302, 41977022) and the Natural Science Foundation of Hubei Province, China (2023AFD227). The authors thank Prof. Yuanzhi Li at Wuhan University of Technology for his help with DFT calculations. The authors also thank Beijing Synchrotron Radiation Facility (BSRF), China, for EXAFS measurements at Beamline 1W1B.

■ REFERENCES

(1) Qiao, J. T.; Liu, J. Y.; Palomo, A.; Bostick, B. C.; Phan, K.; Zheng, Y.; Li, F. B. Prevalence of Methylated Arsenic and Microbial Arsenic Methylation Genes in Paddy Soils of the Mekong Delta. *Environ. Sci. Technol.* **2023**, *57* (26), 9675−9682.

(2) Yuan, Z. F.; Zhou, Y. J.; Chen, Z.; Zhang, T.; Kappler, A.; Gustave, W.; Tang, X. J.; Xu, J. M. Sustainable Immobilization of Arsenic by Man-Made Aerenchymatous Tissues in Paddy Soil. *Environ. Sci. Technol.* **2023**, *57* (33), 12280−12290.

(3) Beaulieu, B. T.; Savage, K. S. Arsenate Adsorption Structures on Aluminum Oxide and Phyllosilicate Mineral Sufaces in Smelter-Impacted Soils. *Environ. Sci. Technol.* **2005**, *39* (10), 3571−3579.

(4) Dwivedi, S.; Tripathi, R. D.; Tripathi, P.; Kumar, A.; Dave, R.; Mishra, S.; Singh, R.; Sharma, D.; Rai, U. N.; Chakrabarty, D.; Trivedi, P. K.; Adhikari, B.; Bag, M. K.; Dhankher, O. P.; Tuli, R. Arsenate Exposure Affects Amino Acids, Mineral Nutrient Status and Antioxidants in Rice (L.) Genotypes. *Environ. Sci. Technol.* **2010**, *44* (24), 9542−9549.

(5) Bylaska, E. J.; Catalano, J. G.; Mergelsberg, S. T.; Saslow, S. A.; Qafoku, O.; Prange, M. P.; Ilton, E. S. Association of Defects and Zinc in Hematite. *Environ. Sci. Technol.* **2019**, *53* (23), 13687−13694.
(6) Huang, X.; Hou, X.; Zhang, X.; Rosso, K. M.; Zhang, L. Facet-Dependent Contaminant Removal Properties of Hematite Nanocrystals and Their Environmental Implications. *Environ. Sci.: Nano* **2018**, *5* (8), 1790−1806.
(7) Tan, W.; Liang, Y.; Xu, Y.; Wang, M. Structural-Controlled Formation of Nano-Particle Hematite and Their Removal Performance for Heavy Metal Ions: A Review. *Chemosphere* **2022**, *306*, No. 135540.
(8) Cornell, R. M.; Schwertmann, U. *The Iron Oxides: Structure, Properties, Reactions, Occurences and Uses*; Wiley-VCH, 2003.
(9) Liang, Y.; Wang, M. X.; Xiong, J.; Hou, J. T.; Wang, X. M.; Tan, W. F. Al-Substitution- Induced Defect Sites Enhance Adsorption of Pb^{2+} on Hematite. *Environ. Sci.: Nano* **2019**, *6* (5), 1323−1331.
(10) Liu, J.; Xiang, Y.; Chen, Y.; Zhang, H.; Ye, B.; Ren, L.; Tan, W.; Kappler, A.; Hou, J. Quantitative Contribution of Oxygen Vacancy Defects to Arsenate Immobilization on Hematite. *Environ. Sci. Technol.* **2023**, *57* (33), 12453−12464.
(11) da Silva Alvim, R.; Ribeiro, F. N.; Dalpian, G. M. Iron and Oxygen Vacancies at the Hematite Surface: Pristine Case and with a Chlorine Adatom. *Phys. Chem. Chem. Phys.* **2020**, *22* (43), 25380−25389.
(12) Ding, T.; Li, Y.; Xu, X.; Li, Z.; Jiao, H.; Na, P.; Ding, Y.; Wang, X. Hydrothermal Carbonization-Induced Oxygen Vacancies on Hematite for Boosting Photo-Fenton Performance. *Chem. Phys. Lett.* **2023**, *826*, No. 140645.
(13) Liang, Y.; Jin, J.; Xiang, Y.; Wang, M.; Xiong, J.; Hou, J.; Tan, W. Insights into the Improving Mechanism of Defect-Mediated As(V) Adsorption on Hematite Nanoplates. *Chemosphere* **2021**, *280*, No. 130597.
(14) Notini, L.; Latta, D. E.; Neumann, A.; Pearce, C. I.; Sassi, M.; N'Diaye, A. T.; Rosso, K. M.; Scherer, M. M. The Role of Defects in Fe(II)−Goethite Electron Transfer. *Environ. Sci. Technol.* **2018**, *52* (5), 2751−2759.
(15) Notini, L.; Byrne, J. M.; Tomaszewski, E. J.; Latta, D. E.; Zhou, Z.; Scherer, M. M.; Kappler, A. Mineral Defects Enhance Bioavailability of Goethite toward Microbial Fe(III) Reduction. *Environ. Sci. Technol.* **2019**, *53* (15), 8883−8891.
(16) Chi, Z. L.; Yu, G. H.; Kappler, A.; Liu, C. Q.; Gadd, G. M. Fungal−Mineral Interactions Modulating Intrinsic Peroxidase-Like Activity of Iron Nanoparticles: Implications for the Biogeochemical Cycles of Nutrient Elements and Attenuation of Contaminants. *Environ. Sci. Technol.* **2022**, *56* (1), 672−680.
(17) Hou, J.; Tan, X.; Xiang, Y.; Zheng, Q.; Chen, C.; Sha, Z.; Ren, L.; Wang, M.; Tan, W. Insights into the Underlying Effect of Fe Vacancy Defects on the Adsorption Affinity of Goethite for Arsenic Immobilization. *Environ. Pollut.* **2022**, *314*, No. 120268.
(18) Jin, X.; Wu, D.; Liu, C.; Huang, S.; Zhou, Z.; Wu, H.; Chen, X.; Huang, M.; Zhou, S.; Gu, C. Facet Effect of Hematite on the Hydrolysis of Phthalate Esters under Ambient Humidity Conditions. *Nat. Commun.* **2022**, *13* (1), No. 6125.
(19) Li, W.; Liang, X.; An, P.; Feng, X.; Tan, W.; Qiu, G.; Yin, H.; Liu, F. Mechanisms on the Morphology Variation of Hematite Crystals by Al Substitution: The Modification of Fe and O Reticular Densities. *Sci. Rep.* **2016**, *6* (1), No. 35960.
(20) Ling, D.; Lee, N.; Hyeon, T. Chemical Synthesis and Assembly of Uniformly Sized Iron Oxide Nanoparticles for Medical Applications. *Acc. Chem. Res.* **2015**, *48* (5), 1276−1285.
(21) Wang, J.; Rustad, J. R. A Simple Model for the Effect of Hydration on the Distribution of Ferrous Iron at Reduced Hematite (012) Surfaces. *Geochim. Cosmochim. Acta* **2006**, *70* (21), 5285−5292.
(22) Catalano, J. G. Weak Interfacial Water Ordering on Isostructural Hematite and Corundum (001) Surfaces. *Geochim. Cosmochim. Acta* **2011**, *75*, 2062−2071.
(23) Noerpel, M. R.; Lee, S. S.; Lenhart, J. J. X-Ray Analyses of Lead Adsorption on the (001), (110), and (012) Hematite Surfaces. *Environ. Sci. Technol.* **2016**, *50* (22), 12283−12291.
(24) Mei, H. Y.; Liu, Y.; Tan, X. L.; Feng, J. H.; Ai, Y. J.; Fang, M. U(VI) Adsorption on Hematite Nanocrystals: Insights into the Reactivity of {001} and {012} Facets. *J. Hazard. Mater.* **2020**, *399*, No. 123028, DOI: 10.1016/j.jhazmat.2020.123028.
(25) Hu, S.; Wu, Y.; Ding, Z.; Shi, Z.; Li, F.; Liu, T. Facet-Dependent Reductive Dissolution of Hematite Nanoparticles by Shewanella Putrefaciens CN-32. *Environ. Sci.: Nano* **2020**, *7* (9), 2522−2531.
(26) Hu, S.; Wu, Y.; Shi, Z.; Li, F.; Liu, T. Quinone-Mediated Dissimilatory Iron Reduction of Hematite: Interfacial Reactions on Exposed {001} and {100} Facets. *J. Colloid Interface Sci.* **2021**, *583*, 544−552.
(27) Wang, S.; Hu, X.; Yu, F.; Qin, S. Microbe Regulates the Mineral Photochemical Activity and Organic Matter Compositions in Water. *Water Res.* **2022**, *225*, No. 119164.
(28) Cao, Y.; Shen, L.; Hu, X.; Du, Z.; Jiang, L. Low Temperature Desulfurization on Co-Doped α-FeOOH: Tailoring the Phase Composition and Creating the Defects. *Chem. Eng. J.* **2016**, *306*, 124−130.
(29) Hong, Z.; Li, F.; Borch, T.; Shi, Q.; Fang, L. Incorporation of Cu into Goethite Stimulates Oxygen Activation by Surface-Bound Fe(II) for Enhanced As(III) Oxidative Transformation. *Environ. Sci. Technol.* **2023**, *57* (5), 2162−2174.
(30) Gonzalez, E.; Ballesteros, M. C.; Rueda, E. H. Reductive Dissolution Kinetics of Al-Substituted Goethites. *Clays Clay Miner.* **2002**, *50* (4), 470−477.
(31) Schwertmann, U.; Carlson, L. Aluminum Influence on Iron Oxides: XVII. Unit-Cell Parameters and Aluminum Substitution of Natural Goethites. *Soil Sci. Soc. Am. J.* **1994**, *58* (1), 256−261.
(32) Hou, J.; Li, Y.; Mao, M.; Ren, L.; Zhao, X. Tremendous Effect of the Morphology of Birnessite-Type Manganese Oxide Nanostructures on Catalytic Activity. *ACS Appl. Mater. Interfaces* **2014**, *6* (17), 14981−14987.
(33) Zheng, Q.; Tu, S.; Chen, Y.; Zhang, H.; Hartley, W.; Ye, B.; Ren, L.; Xiong, J.; Tan, W.; Kappler, A.; Hou, J. Micropore Sites in Ferrihydrite Are Responsible for Its Higher Affinity Towards As(III) Relative to As(V). *Geochim. Cosmochim. Acta* **2023**, *348*, 27−40.
(34) Liu, F.; Lin, X. F. Types of Crystalline Iron Oxides and Phosphate Adsorption in Variable Charge Soils. *Pedosphere* **1994**, *4* (1), 35−46.
(35) Catalano, J. G.; Fenter, P.; Park, C. Interfacial Water Structure on the (012) Surface of Hematite: Ordering and Reactivity in Comparison with Corundum. *Geochim. Cosmochim. Acta* **2007**, *71* (22), 5313−5324.
(36) Catalano, J. G.; Fenter, P.; Park, C. Water Ordering and Surface Relaxations at the Hematite (110)−Water Interface. *Geochim. Cosmochim. Acta* **2009**, *73* (8), 2242−2251.
(37) Fang, L. P.; Gao, B. L.; Li, F. B.; Liu, K.; Chi, J. L. The Nature of Metal Atoms Incorporated in Hematite Determines Oxygen Activation by Surface-Bound Fe(II) for As(III) Oxidation. *Water Res.* **2022**, *227*, No. 119351.
(38) Yan, L.; Chan, T. S.; Jing, C. Y. Arsenic Adsorption on Hematite Facets: Spectroscopy and DFT Study. *Environ. Sci.: Nano* **2020**, *7* (12), 3927−3939.
(39) Fang, L.; Hong, Z.; Borch, T.; Shi, Q.; Li, F. Iron Vacancy Accelerates Fe(II)-Induced Anoxic As(III) Oxidation Coupled to Iron Reduction. *Environ. Sci. Technol.* **2023**, *57* (5), 2175−2185.
(40) Hong, Z. B.; Fang, L. P.; Zhong, S. X.; Liu, K.; Li, F. B. Fe(II)-Mediated Activation of Oxygen by Goethite for the As(III) Oxidation and the Mechanisms. *Chin. Sci. Bull.* **2020**, *65* (11), 997−1008.
(41) Jain, N.; Maiti, A. Fe-Mn-Al Metal Oxides/Oxyhydroxides as As(III) Oxidant under Visible Light and Adsorption of Total Arsenic in the Groundwater Environment. *Sep. Purif. Technol.* **2022**, *302*, No. 122170.
(42) Ren, L.; Zhong, Y. H.; Xu, J. Y.; Chen, J. X.; Zou, T.; Liao, X. L.; Chen, Z. F.; Yu, L. Nano $Fe_{3-X}Cu_xO_4$ as the Heterogeneous

Catalyst in an Advanced Oxidation Process for Excellent Peroxymonosulfate Activation toward Climbazole Degradation. *Chem. Eng. J.* **2022**, *439*, No. 135553.
(43) Ogorodnikova, O. V.; Majerle, M.; Čížek, J.; Simakov, S.; Gann, V. V.; Hruška, P.; Kameník, J.; Pospíšil, J.; Štefánik, M.; Vinš, M. Positron Annihilation Spectroscopy Study of Radiation-Induced Defects in W and Fe Irradiated with Neutrons with Different Spectra. *Sci. Rep.* **2020**, *10* (1), No. 18898.
(44) Avachat, A. V.; Mahmoud, K. H.; Leja, A. G.; Xu, J. J.; Anastasio, M. A.; Sivaguru, M.; Di Fulvio, A. Ortho-Positronium Lifetime for Soft-Tissue Classification. *Sci. Rep.* **2024**, *14* (1), No. 21155.
(45) Van Genuchten, C. M.; Addy, S. E. A.; Peña, J.; Gadgil, A. Removing Arsenic from Synthetic Groundwater with Iron Electrocoagulation: An Fe and As K-Edge EXAFS Study. *Environ. Sci. Technol.* **2012**, *46* (2), 986−994.
(46) Wan, D.; Liu, F. F.; Chen, J. B.; Kappler, A.; Kuzyakov, Y.; Liu, C. Q.; Yu, G. H. Microbial Community Mediates Hydroxyl Radical Production in Soil Slurries by Iron Redox Transformation. *Water Res.* **2022**, *220*, No. 118689.
(47) Huang, X.; Hou, X.; Song, F.; Zhao, J.; Zhang, L. Facet-Dependent Cr(VI) Adsorption of Hematite Nanocrystals. *Environ. Sci. Technol.* **2016**, *50* (4), 1964−1972.
(48) Wang, W.; Zhang, W.; Fan, Y.; Qu, C.; Ren, W.; Huang, X.; Hong, M.; Liu, F.; Yin, H. Facet-Dependent Adsorption of Aluminum(III) on Hematite Nanocrystals and the Influence on Mineral Transformation. *Environ. Sci.: Nano* **2022**, *9* (6), 2073−2085.
(49) Sun, S.; Zhai, T.; Liang, C.; Savilov, S. V.; Xia, H. Boosted Crystalline/Amorphous $Fe_2O_{3-\delta}$ Core/Shell Heterostructure for Flexible Solid-State Pseudocapacitors in Large Scale. *Nano Energy* **2018**, *45*, 390−397.
(50) Yan, L.; Chan, T. S.; Jing, C. Y. Mechanistic Study for Antimony Adsorption and Precipitation on Hematite Facets. *Environ. Sci. Technol.* **2022**, *56* (5), 3138−3146.
(51) Zhang, J.; Jing, B.; Tang, Z.; Ao, Z.; Xia, D.; Zhu, M.; Wang, S. Experimental and DFT Insights into the Visible-Light Driving Metal-Free C_3N_5 Activated Persulfate System for Efficient Water Purification. *Appl. Catal., B* **2021**, *289*, No. 120023.
(52) Tang, X.; Chen, J.; Chen, Y. A Density Functional Based Tight Binding (DFTB+) Study on the Sulfidization-Xanthate Flotation Mechanism of Cerussite. *Appl. Surf. Sci.* **2023**, *612*, No. 155677.
(53) Yan, L.; Chan, T.; Jing, C. Arsenic Adsorption on Hematite Facets: Spectroscopy and DFT Study. *Environ. Sci.: Nano* **2020**, *7* (12), 3927−3939.
(54) Yan, L.; Chan, T.; Jing, C. Mechanistic Study for Antimony Adsorption and Precipitation on Hematite Facets. *Environ. Sci. Technol.* **2022**, *56* (5), 3138−3146.
(55) van Santen, R. A.; Tranca, I. How Molecular Is the Chemisorptive Bond? *Phys. Chem. Chem. Phys.* **2016**, *18* (31), 20868−20894.
(56) Fung, V.; Wu, Z.; Jiang, D. E. New Bonding Model of Radical Adsorbate on Lattice Oxygen of Perovskites. *J. Phys. Chem. Lett.* **2018**, *9* (21), 6321−6325.
(57) Zhang, H. J.; Sellaiyan, S.; Kakizaki, T.; Uedono, A.; Taniguchi, Y.; Hayashi, K. Effect of Free-Volume Holes on Dynamic Mechanical Properties of Epoxy Resins for Carbon-Fiber-Reinforced Polymers. *Macromolecules* **2017**, *50* (10), 3933−3942.
(58) Takahashi, S.; Brunel, L. C.; Edwards, D. T.; van Tol, J.; Ramian, G.; Han, S.; Sherwin, M. S. Pulsed Electron Paramagnetic Resonance Spectroscopy Powered by a Free-Electron Laser. *Nature* **2012**, *489* (7416), 409−413.
(59) Bonke, S. A.; Risse, T.; Schnegg, A.; Brückner, A. In Situ Electron Paramagnetic Resonance Spectroscopy for Catalysis. *Nat. Rev. Methods Primers* **2021**, *1* (1), 33.
(60) Savchenko, D.; Vasin, A.; Kuz, O.; Verovsky, I.; Prokhorov, A.; Nazarov, A.; Lančok, J.; Kalabukhova, E. Role of the Paramagnetic Donor-Like Defects in the High N-Type Conductivity of the Hydrogenated ZnO Microparticles. *Sci. Rep.* **2020**, *10* (1), No. 17347.
(61) Biswas, P.; Ainabayev, A.; Zhussupbekova, A.; Jose, F.; O'Connor, R.; Kaisha, A.; Walls, B.; Shvets, I. V. Tuning of Oxygen Vacancy-Induced Electrical Conductivity in Ti-Doped Hematite Films and Its Impact on Photoelectrochemical Water Splitting. *Sci. Rep.* **2020**, *10* (1), No. 7463.
(62) Huang, Y. C.; Li, K. S.; Li, S. Q.; Lin, Y.; Liu, H.; Tong, Y. X. Ultrathin Bi_2MOO_6 Nanosheets for Photocatalysis: Performance Enhancement by Atomic Interfacial Engineering. *ChemistrySelect* **2018**, *3* (26), 7423−7428.
(63) Ma, L.; Cheng, Y. S.; Cavataio, G.; McCabe, R. W.; Fu, L. X.; Li, J. H. In situ DRIFTS and temperature-programmed technology study on NH_3-SCR of NO_x over Cu-SSZ-13 and Cu-SAPO-34 catalysts. *Appl. Catal., B* **2014**, *156*−*157*, 428−437.
(64) Sjövall, H.; Fridell, E.; Blint, R. J.; Olsson, L. Identification of Adsorbed Species on Cu-ZSM-5 under NH_3 SCR Conditions. *Top. Catal.* **2007**, *42*−*43* (1), 113−117.
(65) Wang, D.; Zhang, L.; Kamasamudram, K.; Epling, W. S. In Situ-Drifts Study of Selective Catalytic Reduction of Nox by NH_3 over Cu-Exchanged SAPO-34. *ACS Catal.* **2013**, *3* (5), 871−881.
(66) Ona-Nguema, G.; Morin, G.; Juillot, F.; Calas, G.; Brown, G. E. EXAFS Analysis of Arsenite Adsorption onto Two-Line Ferrihydrite, Hematite, Goethite, and Lepidocrocite. *Environ. Sci. Technol.* **2005**, *39* (23), 9147−9155.
(67) McBriarty, M. E.; Stubbs, J. E.; Eng, P. J.; Rosso, K. M. Potential-Specific Structure at the Hematite−Electrolyte Interface. *Adv. Funct. Mater.* **2018**, *28* (8), No. 1705618.
(68) McBriarty, M. E.; von Rudorff, G. F.; Stubbs, J. E.; Eng, P. J.; Blumberger, J.; Rosso, K. M. Dynamic Stabilization of Metal Oxide−Water Interfaces. *J. Am. Chem. Soc.* **2017**, *139* (7), 2581−2584.
(69) Li, M. Y.; Ye, K. H.; Qiu, W. T.; Wang, Y. F.; Ren, H. Heterogeneity between and within Single Hematite Nanorods as Electrocatalysts for Oxygen Evolution Reaction. *J. Am. Chem. Soc.* **2022**, *144* (12), 5247−5252.
(70) Chen, S.; Li, J.; Zhou, W.; Yi, G.; Wei, Z.; Chang, Y.; Huang, D. Engineering Defects in Heterogeneous Catalytic Persulfates for Water Purification: An Overlooked Role? *Coord. Chem. Rev.* **2024**, *507*, No. 215749.
(71) Dong, W.; Xiao, H.; Jia, Y.; Chen, L.; Geng, H.; Bakhtiar, S. U. H.; Fu, Q.; Guo, Y. Engineering the Defects and Microstructures in Ferroelectrics for Enhanced/Novel Properties: An Emerging Way to Cope with Energy Crisis and Environmental Pollution. *Adv. Sci.* **2022**, *9* (13), No. 2105368.
(72) Hao, T.; Huang, Y.; Li, F.; Wu, Y.; Fang, L. Facet-Dependent Fe(II) Redox Chemistry on Iron Oxide for Organic Pollutant Transformation and Mechanisms. *Water Res.* **2022**, *219*, No. 118587.
(73) Patra, A. K.; Kundu, S. K.; Bhaumik, A.; Kim, D. Morphology Evolution of Single-Crystalline Hematite Nanocrystals: Magnetically Recoverable Nanocatalysts for Enhanced Facet-Driven Photoredox Activity. *Nanoscale* **2016**, *8* (1), 365−377.

https://doi.org/10.1021/acs.est.4c11344
Environ. Sci. Technol. 2025, 59, 2802−2814